



저작자표시-변경금지 2.0 대한민국

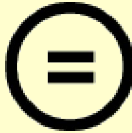
이용자는 아래의 조건을 따르는 경우에 한하여 자유롭게

- 이 저작물을 복제, 배포, 전송, 전시, 공연 및 방송할 수 있습니다.
- 이 저작물을 영리 목적으로 이용할 수 있습니다.

다음과 같은 조건을 따라야 합니다:



저작자표시. 귀하는 원저작자를 표시하여야 합니다.



변경금지. 귀하는 이 저작물을 개작, 변형 또는 가공할 수 없습니다.

- 귀하는, 이 저작물의 재이용이나 배포의 경우, 이 저작물에 적용된 이용허락조건을 명확하게 나타내어야 합니다.
- 저작권자로부터 별도의 허가를 받으면 이러한 조건들은 적용되지 않습니다.

저작권법에 따른 이용자의 권리는 위의 내용에 의하여 영향을 받지 않습니다.

이것은 [이용허락규약\(Legal Code\)](#)을 이해하기 쉽게 요약한 것입니다.

[Disclaimer](#)

공학석사 학위논문

Influence of Ribs on Internal Heat Transfer and Pressure Drop in a Turbine Blade Trailing Edge Channel

가스터빈 블레이드 후연 채널에서 내부 열전달 및
압력강하에 대한 립의 영향

2020 년 2 월

서울대학교 대학원

기계항공공학부

김 수 현

Abstract

Convective cooling inside the internal passage of a turbine blade trailing edge is often insufficient at the sharp corner, when cutback slot cooling is not present. This study investigates the convective heat transfer and pressure drop in a simplified trailing edge internal channel. The internal passage has been modeled as a right triangular channel with a 9° angle sharp corner. Heated baseline (with no internal features) and ribbed copper plates have been examined via infrared thermography. A uniform heat flux heater is installed beneath the plates, and non-uniformities in the heat flux due to conduction is corrected by a RANS conjugate heat transfer calculation. The numerical simulations were validated beforehand by experimental results of mean velocity, friction factor, and temperature fields.

Nusselt number distributions show that convective heat transfer is significantly enhanced with ribs, and closely coupled with the vortical flow structure. Heat transfer at the corner is increased with ribs, due to a combination of flow blockage effect from the ribs, and secondary flow towards the corner. Although the pressure loss and friction increase slightly, the overall thermal performance, represented by the average Nusselt number with respect to the friction factor, increases by a factor of two with the ribs.

Keyword : Gas turbine blade, Trailing edge, Sharp edge, Triangular channel, heat transfer, Rib turbulators

Student Number : 2018–23025

Table of Contents

| | |
|--|-----------|
| Abstract | i |
| Contents..... | ii |
| List of Figures | iii |
| List of Tables..... | v |
| Nomenclature..... | vi |
| Chapter 1. Introduction..... | 1 |
| 1.1 Research background | 1 |
| 2.1 Purpose of research | 5 |
| Chapter 2. Experimental method | 6 |
| 2.1 Experimental setup..... | 6 |
| 2.2 Temperature calibration | 8 |
| 2.2 Data Reduction..... | 9 |
| Chapter 3. Numerical method | 17 |
| 3.1 Computational setup | 17 |
| 3.2 Validation..... | 21 |
| Chapter 4. Results and Discussion | 28 |
| 4.1 Heat transfer..... | 28 |
| 4.2 Pressure losses | 36 |
| 4.3 Thermal performance..... | 37 |
| 4.4 Uncertainty..... | 38 |
| Chapter 5. Conclusion..... | 45 |
| Acknowledgment | 47 |
| Bibliography | 48 |
| Abstract in Korean | 53 |

List of Figures

| | |
|---|----|
| FIGURE 2.1 Schematic of experimental setup | 13 |
| FIGURE 2.2 Baseline and ribbed channel geometry | 13 |
| FIGURE 2.3 Rib geometry in the ribbed | 14 |
| FIGURE 2.4 Triangular cross-section test section. | 15 |
| FIGURE 2.5 Configuration of measurement | 16 |
| FIGURE 3.1 Thermal boundary conditions | 24 |
| FIGURE 3.2 Results of grid dependency test | 25 |
| FIGURE 3.3 Centerline streamwise velocity for the baseline channel | 26 |
| FIGURE 3.4 Centerline streamwise velocity for ribbed channel..... | 26 |
| FIGURE 3.5 Wall shear stress distribution in ribbed channel..... | 27 |
| FIGURE 4.1 Non-dimensional temperature distribution in the baseline channel..... | 39 |
| FIGURE 4.2 Averaged Nusselt number along streamwise direction in baseline channel | 40 |
| FIGURE 4.3 Averaged Nusselt number in baseline channel at fully developed region | 40 |
| FIGURE 4.4 Local Nusselt number contour in ribbed channel | 41 |

| | |
|---|----|
| FIGURE 4.5 Local Nusselt number distribution between the ribs..... | 42 |
| FIGURE 4.6 Vortex core region in ribbed channel near the ribs | 42 |
| FIGURE 4.7 2D distribution of swirling strength in ribbed channel | 43 |
| FIGURE 4.8 Normalized averaged Nusselt number near the sharp edge | 43 |
| FIGURE 4.9 Friction factor in baseline and ribbed channel..... | 44 |

List of Tables

| | |
|--|----|
| TABLE 2.1 Channel cross-section and rib geometry | 15 |
| TABLE 4.1 Thermal performance in ribbed channel | 44 |

Nomenclature

| | |
|-----------------|--|
| α | Rib angle |
| A | Area of heated surface |
| c_p | Specific heat capacity |
| D_h | Hydraulic diameter |
| f | Friction factor |
| F | Thermal performance |
| H | Channel height |
| h | Heat transfer coefficient |
| h_{rib} | Rib height |
| k | Thermal conductivity |
| L | Channel length |
| l | Rib length |
| \dot{m} | Bulk mass flow rate |
| Nu | Nusselt number |
| Nu ₀ | Nusselt number from Dittus-Boelter |
| P | Pressure |
| p | Rib pitch |
| Q | Total heat from heater |
| q_s'' | Uniform heat flux from the heat source |
| Re | Reynolds number |
| S | Heat sink |
| T | Temperature |
| T_m | Bulk temperature (mass flow averaged) |
| \tilde{T} | Residual temperature |

| | |
|------------|--|
| U | Average fluid velocity |
| u | Velocity |
| u_z | Streamwise velocity |
| V | Spanwise velocity |
| W | Channel width |
| w | Rib width |
| x | Spanwise position |
| z | Streamwise position |
| ρ | Fluid density |
| θ | Non-dimensional temperature |
| θ | Apex angle |
| τ_w | Wall shear stress |
| $()_{CL}$ | Coordinate along the centerline of the channel cross-section |

Chapter 1. Introduction

1.1. Research Background

Gas turbine thermal efficiency and power output highly depend on the inlet temperature. The development of gas turbines thus aims to increase the inlet temperature. However, the inlet temperature in modern gas turbines already exceeds the allowable limit of the component materials. In order to ensure that the turbine blades can survive in such extreme temperatures, various blade cooling techniques such as rib turbulators and film cooling have been developed over the last few decades.

Blade trailing edges are one of the most difficult regions to apply cooling techniques, due to the thin airfoil [1]. Many studies have examined both external and internal cooling schemes. The most representative method is a combination of internal pin-fin and external slot cooling [2, 3]. Horbach et al. [4] studied external cooling performance of a pin-fin configuration in trailing edge cutback film cooling. Martini et al. [5, 6] experimentally and numerically examined film cooling performance of a trailing edge cutback with various internal cooling designs. Schneider et al. [7] analyzed root-

mean-square (RMS) velocity profiles and film-cooling effectiveness in trailing edge cutback using large-eddy simulations (LES).

Despite much research on external cooling of blade trailing edges, these cooling methods still have some disadvantages. Cooling using a pin-fin pedestal array combined with cutback slots can lead to large thermal stress due to the temperature difference between the pressure and suction sides of the blade [3]. Ejection of air for external cooling also deteriorates the aerodynamic performance of the blade, which leads to a decrease in thermal efficiency of the turbine.

Some researchers have studied heat transfer, pressure drop, and flow structure in isosceles triangle channels with small apex angles, which are similar in geometry to trailing edge internal cooling channels with a sharp edge. Eckert and Irvine [8] experimentally analyzed heat transfer characteristics and pressure drop in a triangular channel with an apex angle of 11.48° . Leung et al. [9] experimentally derived an equation of averaged Nusselt number for a triangular channel, in terms of Reynolds number and apex angle between 15° and 90° . Pressure drop and friction factor for triangular channels with small apex angles were investigated by various

studies [10, 11], and compared to a circular pipe. Daschiel et al. [12] numerically investigated flow in the same triangular channel as Eckert using direct numerical simulation (DNS).

Baek et al. [13] experimentally and numerically investigated flow in two right triangular channels (with and without ribs) of 9° apex angle using magnetic resonance velocimetry (MRV) and LES. The results without ribs showed a dramatic decrease of the flow in the narrow corner, which would subsequently reduce heat transfer at the sharp edge. Installing oblique ribs increased the flow velocity near the corner. Therefore, rib turbulators can be used as an effective internal cooling technique in the blade trailing edge.

Many studies have examined heat transfer in a channel with various rib geometries. Ahn et al. [14] investigated the flow structure and heat transfer coefficient in a 90° ribbed square channel with two different rib geometries via experiments and LES. The results showed that the flow reattachment and vortex structures due to the ribs had an effect on the heat transfer characteristics. Astrita and Cardone [15] experimentally studied heat transfer characteristics in a U-bend channel with 45° angle square ribs. They also examined the local Nusselt number distribution due to flow reattachment and

secondary flow. Tanda [16] mapped the local heat transfer coefficient in a square channel with 45° angle square ribs using liquid crystal thermography. Heat transfer in channels with various rib geometries and angles have been conducted by various studies [17, 18]. Moreover, several studies dedicated to finding the correlation for Nusselt number and friction factor for various rib characteristics are being conducted [19, 20].

Only a small number of previous research on heat transfer in ribbed narrow triangular channels exist. Naik et al. [1] and Saxer-Felici et al. [21] experimentally measured the heat transfer coefficient in a triangular ribbed channel using thermochromic liquid crystals (TLC). Coletti et al. [22] investigated non-dimensional temperature and Nusselt number distributions of various rib materials in a trapezoidal channel using infrared thermography.

Studies investigating heat transfer in ribbed channels typically use low conductivity materials or thin foil for the heated surfaces to minimize lateral heat flux due to conduction. Various methods are employed for conduction correction. Won [23] fabricated a test section using acrylic with low conductivity and performed a conduction analysis using ANSYS with experimentally measured boundary temperature. Coletti et al. [22] did not

implement the thin foil technique, but made corrections for the uniform heat flux using 2D finite element method (FEM) based on the experimentally measured temperature field.

1.2. Purpose of Research

This study presents an experimental investigation of the heat transfer and pressure drop in a triangular channel, with and without ribs, using a mid-wave infrared (MWIR) camera. In addition, a new method of conduction correction using Reynolds averaged Navier-Stokes (RANS) simulations is introduced, after the CFD method has been validated using the flow structure. These results exemplify the laminarization at the sharp corner, and show how the heat transfer can be enhanced by installing oblique ribs pointing away from the corner.

Chapter 2. Experimental Setup & Procedure

2.1. Experimental setup

A schematic of the experimental setup is shown in figure 2.1. The test section is placed inside an open-loop wind tunnel. A converging section is attached in front of the test section to allow air to enter uniformly. The converging section has an inlet-to-outlet area ratio of 3:1, and the end of the converging section has the same shape as the triangular test section. The flow rate is calculated by integrating the velocity at 800 points at the outlet, measured by a pitot probe.

The present study deals with two right triangular channels, the baseline channel without ribs, and a ribbed channel with 45° rectangular ribs. The geometries of both channels are shown in figure 2.2. The details of their configurations are shown in figure 2.3 and Table 2.1.

Figure 2.4 shows a detailed view of the test section. The total length of the channel, L , is 710 mm. In front of the test section, a flow development channel with 135 mm length ($= 10 D_h$) is placed to obtain hydrodynamically fully developed flow at the end of the test section. The overall test section is

machined out of 20 mm thick acrylic. The heated baseline and ribbed surfaces are made out of 5 mm thick copper plates. The reason why the plates are thick is because they are machined as one piece (i.e., the ribs are not separately attached), and the thickness was necessary to prevent plate warping. To measure the temperature field of the heated surface, three sections are machined out from the top plate of the test section, and sapphire windows with anti-reflection coating are inserted. The wind tunnel is covered with a black drape to remove reflections on the optical window. The test section is covered with fiberglass to minimize heat loss.

Figure 2.5 displays the configuration of the measurement system. The temperature of the heated surface is measured via infrared thermography by a FLIR A6750SC MWIR camera. The target surface is thinly coated with Armeco high emissivity black paint. Six K-type thermocouples, two thermocouples for each section, are embedded into the copper plate 0.5 mm, beneath the top of the heated surface. Additionally, two more thermocouples are used to measure the inlet and outlet flow temperature. Constant heat flux of 1200 W/m^2 is applied to the copper plate by two flexible Watlow silicon heaters. Under the heater, a heat reflection coating is applied to minimize heat

loss. Heat reflective insulation is additionally installed before the bottom acrylic surface.

The pressure drop between the inlet and outlet is measured using a Scanivalve DSA3217 pressure scanner. There are 16 static pressure taps arranged at 36.5 mm intervals on the side of the test section, each connected to the pressure scanner.

2.2. Temperature calibration

A FLIR MWIR camera measures the temperature of the plate. The calibration curve for converting raw counts into temperature depends on the temperature range and surface emissivity. Therefore, it is essential to properly calibrate the camera based on the test conditions.

First, a two-point non-uniform calibration (NUC) is performed within the temperature range. Next, temperature calibration is performed using a Fluke 4181 wide aperture blackbody, which has an emissivity of 0.95 and an operating range of -15°C to 500°C . The final equation for converting the counts to temperature utilizes the emissivity value of 0.96 for the black paint used in the experiment.

A separate experiment is conducted to verify that the calibration is done properly. The copper plate is heated from 25°C to 50°C, which encompasses the actual experimental thermal conditions. The temperature values from the calibration match those from the thermocouples installed under the copper plate, to within 0.2°C.

2.3. Data Reduction

The Reynolds number is defined as

$$\text{Re} = \frac{\rho U D_h}{\mu} \dots\dots\dots \text{Equation 2.1}$$

where ρ is the air density, U is the average air velocity, D_h is the hydraulic diameter of the triangular channel, and μ is the air dynamic viscosity. The average streamwise velocity is measured by a pitot tube at the exit of the test section. The local velocity is obtained at intervals of 1 mm in the x direction and 0.5 mm in the y direction, using a traverse. A total of 875 data points are measured for each case (i.e. 6 cases for the baseline channel and 3 cases for the ribbed channel).

The local heat transfer coefficient h is calculated in terms of the heat flux per unit area q'' , and the difference between the local surface temperature and the bulk air temperature. The local heat transfer coefficient and heat flux per unit area can be written as

$$h = \frac{q''}{T_{surface} - T_{air}} \dots\dots\dots \text{Equation 2.2}$$

$$q'' = \frac{Q}{A} \dots\dots\dots \text{Equation 2.3}$$

As mentioned earlier, the heated copper plate, which has high thermal conductivity, is relatively thick. Therefore, a 2D conduction correction is applied to the uniform heat flux distribution, using CFD which was validated by experimental results, as will be discussed again later.

Heated surface temperature is measured by the MWIR camera. The camera counts are averaged over 100 frames. Various errors are corrected for, including misalignment error, black paint non-uniformity error, and optical window error. Sub-pixel misalignment error is caused by slight shaking of the test section during the experiment, and is corrected for by applying a median filter. Black paint non-uniformity error is caused by uneven paint finishes,

and is corrected for using a copper plate heated to a constant temperature. The sapphire window error is relatively small, and is corrected for based on images taken with and without the window. In this study, the bulk temperature range is between 27°C and 30°C. Therefore, correction for hot optical windows, discussed by Gustavsson et al. [24], can be neglected.

The bulk air temperature inside the test section is determined from two thermocouples, one to measure the temperature at the inlet, and the other to measure the temperature at the beginning and end of section 3. The bulk local temperature is estimated by two linear interpolations, one between the inlet to the beginning of section 3, and the other between the beginning and end of section 3. The reason for the separate interpolation for section 3 is to confirm that the flow has become hydraulically and thermally fully developed.

Convective heat transfer is evaluated via the non-dimensional temperature and the local Nusselt number, which are reciprocals of each other:

$$\Theta = \frac{q''}{T_{surface} - T_{air}} \dots\dots\dots \text{Equation 2.4}$$

$$Nu = \frac{hD_h}{k_{air}} = \frac{q''D_h}{k_{air}(T_{surface} - T_{air})} \dots\dots\dots \text{Equation 2.5}$$

In order to normalize the Nusselt number, the smooth channel Nusselt number obtained by Dittus-Boelter's correlation is used:

$$Nu_0 = 0.024Re^{0.8}Pr^{0.4} \dots\dots\dots Equation 2.6$$

The friction factor is obtained from the pressure drop as:

$$f = \frac{2D_h \Delta P}{\rho u^2 L_p} \dots\dots\dots Equation 2.7$$

where ΔP is the average pressure drop along the test section, and L_p is the distance between the first and last pressure taps. In this study, $\left| \frac{dP}{dx} \right|$ is used instead of $\frac{\Delta P}{L_p}$. It is the slope of the linear regression of the static pressure in the streamwise direction, which is measured by 16 pressure taps along the test section.

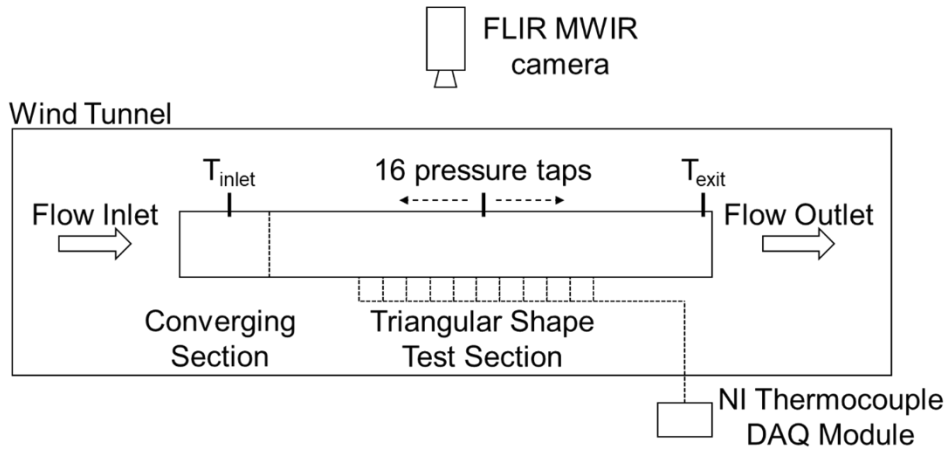


Figure 2.1 Schematic of experimental setup

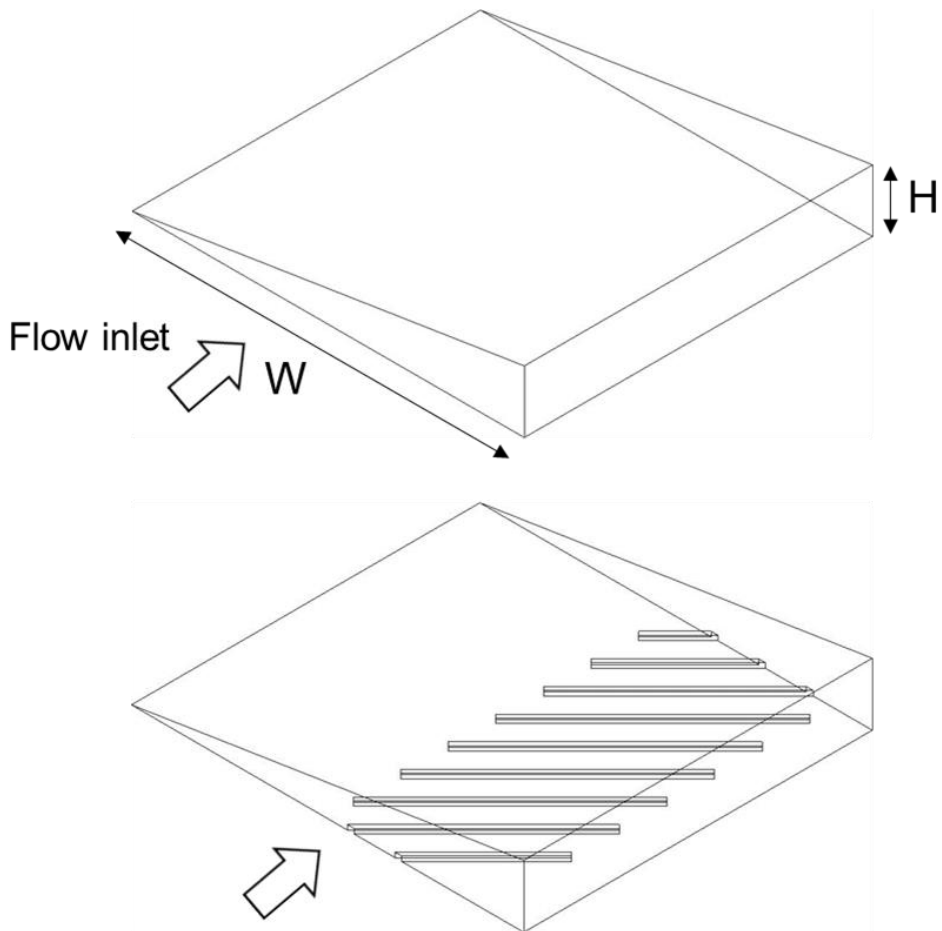


Figure 2.2 Baseline and ribbed channel geometry

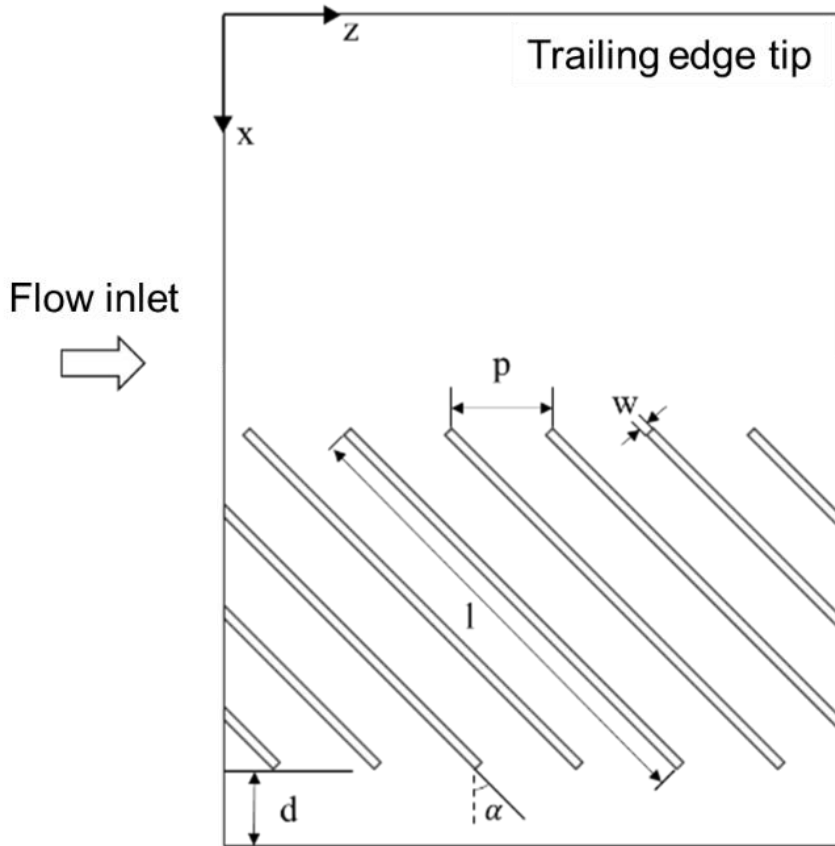


Figure 2.3 Rib geometry in the ribbed channel

Table 2.1 Channel cross-section and rib geometry

| Cross Sectional Geometry | |
|--------------------------------------|----------------|
| Section shape | Right triangle |
| Apex angle (θ) | 9.0° |
| Channel width (W) | 92.3 mm |
| Channel height (H) | 14.6 mm |
| Channel length (L) | 710 mm |
| Hydraulic diameter (D_h) | 13.5 mm |
| Rib Geometry | |
| Rib width (w) | 1.12 mm |
| Rib pitch (p) | 11.2 mm |
| Rib height (h_{rib}) | 1.12 mm |
| Rib length (l) | 52.2 mm |
| Rib angle (α) | 45° |
| Distance from the vertical plate (d) | 8.7 mm |
| Shape of rib end | 90° edges |

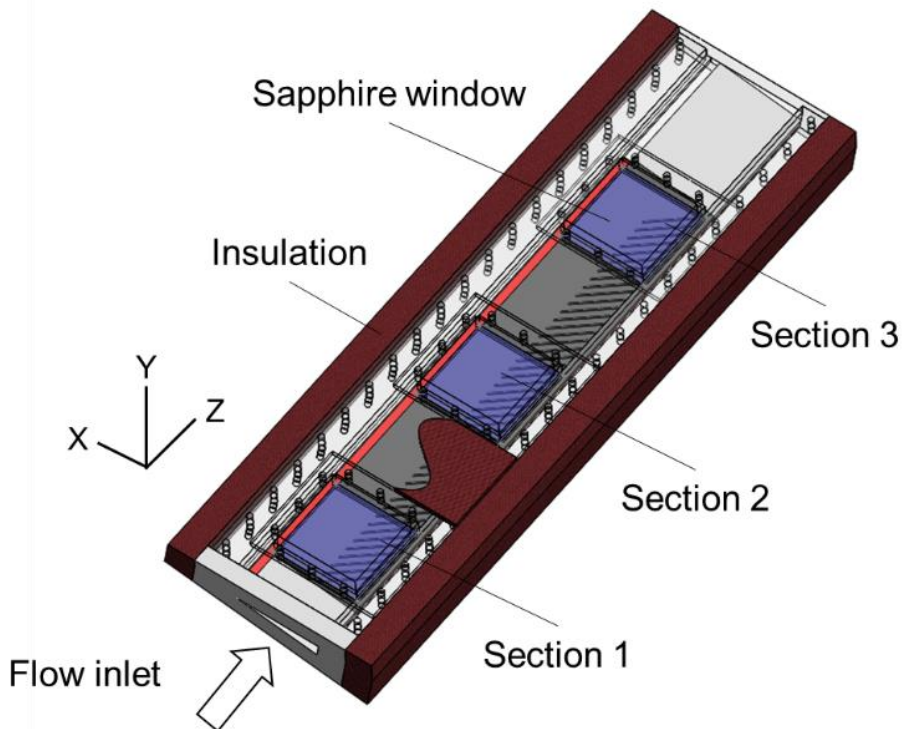


Figure 2.4 Triangular cross-section test section

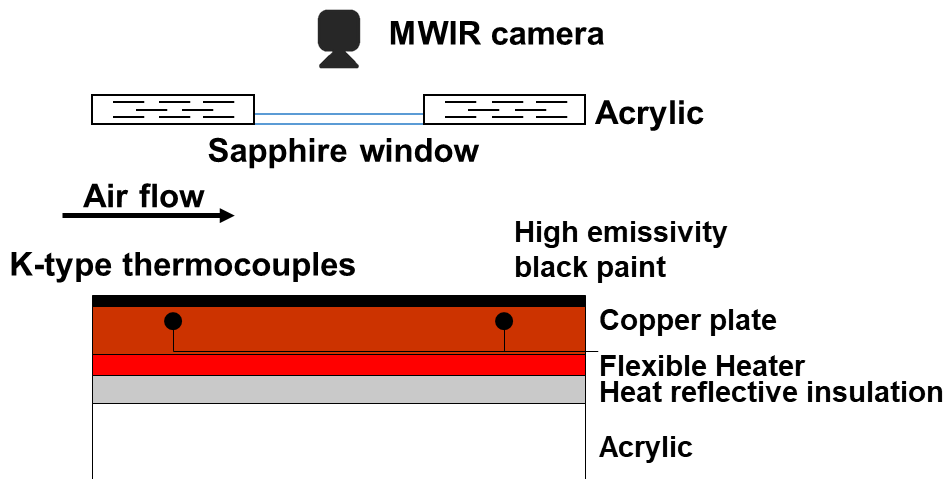


Figure 2.5 Configuration of measurement system

Chapter 3. Numerical Method

3.1. Computational setup

Numerical simulations of the conjugate heat transfer in the test section were conducted by Seungwon Suh, using ANSYS CFX 19.2, to provide local heat flux values on the top surface of the copper plate, which cannot be directly measured from the experiment. Air properties are considered constant, at room temperature of 25°C. The mass flow rate is also held constant. The Baseline Reynolds Stress turbulence model is used since it best predicts both streamwise velocity and secondary flow profiles within the channel [13]. A high-resolution scheme was used for both advection and turbulence, as it prevents oscillatory behavior of the solution, while maintaining accuracy.

The thermal boundary conditions are illustrated in figure 3.1. The heat flux from the electrical heater is assumed to be uniform, and thus uniform heat flux is applied at the bottom of the copper plate. Heat loss through the low conductivity acrylic walls is assumed to be relatively small, and thus the outermost walls are set as adiabatic. Periodic boundary conditions in the streamwise direction are used to save computational time and obtain fully

developed solutions. For the baseline case, the streamwise length of the computational domain is set as 50 mm. For the ribbed case, the length is set such that one whole rib is included in the computational domain.

In a fully developed flow with constant heat flux assigned as boundary conditions, temperature rises linearly in the streamwise direction. Hence, it is impossible to obtain a converged solution under the prescribed thermal boundary conditions, and some preliminary studies handled this problem with a simple mathematical manipulation. Following the procedure of Kawamura et al. [25], Lee et al. [26] decomposed the local temperature into two parts: a linearly increasing term in the streamwise direction, and a residual term,

$$T = \frac{dT_m}{dz}z + \tilde{T} \dots\dots\dots \text{Equation 3.1}$$

where T is the local temperature, T_m is the average fluid bulk temperature, z is the streamwise position, and \tilde{T} is the residual (or ‘fully developed’) temperature. We also implemented this strategy to neglect the linearly increasing part and arrive at a ‘fully developed’ temperature.

The governing energy equation for temperature is

$$\rho c_p \left(\frac{\partial T}{\partial t} + (\vec{u} \cdot \nabla) \tilde{T} \right) = k \nabla^2 T \dots \dots \dots \text{Equation 3.2}$$

In order to obtain \tilde{T} from ANSYS CFX, this governing equation must be modified. By substituting Eq. 3.1 into Eq. 3.2, we obtain a modified energy equation:

$$\rho c_p \left(\frac{\partial T}{\partial t} + (\vec{u} \cdot \nabla) \tilde{T} \right) = k \nabla^2 \tilde{T} - \rho c_p \frac{dT_m}{dz} u_z \dots \dots \dots \text{Equation 3.3}$$

where u_z is the local streamwise velocity. Using the energy balance equation on the computational domain, the streamwise gradient of the mean temperature can be calculated as:

$$\frac{dT_m}{dz} = \frac{q_s'' W}{\dot{m} c_p} \dots \dots \dots \text{Equation 3.4}$$

where q_s'' is the uniform heat flux from the heater, W is the width of the heated channel, and \dot{m} is the bulk mass flow rate. If we define a heat sink as below:

$$S = -\frac{\rho q_s'' W}{\dot{m}} u_z \dots \dots \dots \text{Equation 3.5}$$

the residual temperature \tilde{T} can be found from:

$$\rho c_p \left(\frac{\partial \tilde{T}}{\partial t} + (\vec{u} \cdot \nabla) \tilde{T} \right) = k \nabla^2 \tilde{T} + S \dots \dots \dots \text{Equation 3.6}$$

and its value converges, unlike the original temperature T .

Unstructured grids are used for both fluid and solid domains, and grid dependency is checked using the Darcy friction factor and average Nusselt number. Three different grids are tested for both baseline and ribbed cases: coarse, medium, and fine grids. Both parameters roughly converge at the medium grid for both cases, as shown in figure 3.2. The fine grid of approximately 10 million and 15 million elements are ultimately used for the baseline and ribbed cases, respectively. Five to seven inflation layers are placed near the wall to resolve the boundary layer, as required for the turbulence model used. As a result, y^+ values were maintained below 1 for the baseline case, and below 3 for the ribbed case.

3.2. Validation

We solve both fluid and solid domains simultaneously, unlike Coletti et al. [22] or Won [23], who considered only the solid domain when performing numerical analysis to obtain the heat flux distribution. While only the energy equation is solved in the solid domain, both momentum and energy equations are solved in the fluid domain. Hence, the RANS flow field should be validated using reference data. Data obtained via magnetic resonance velocimetry (MRV) and large eddy simulation (LES) from Baek et al. [13] are used as the reference. The geometry of the baseline test section is identical to ours. For the ribbed case, ribs were installed on both the pressure and suction sides of the channel for Baek et al. [13], whereas only one wall has ribs in our case, due to the need to install optical windows on the other wall. It should be noted that Reynolds numbers based on the hydraulic diameter are 18,400 and 12,000 in the current baseline and ribbed cases, respectively. However, they were slightly different in the previous work: Reynolds numbers were 20,000 and 14,000 for the baseline and ribbed cases, respectively.

To validate the flow field of the baseline case, streamwise velocity

profiles along the centerline of the channel cross-section are compared in figure 3.3. The RANS profile showed good agreement with the MRV and LES data, with a peak near $x/L = 0.9$. Laminarization near the sharp edge is also successfully predicted by RANS.

Streamwise velocity profiles along the centerline are also compared for the ribbed cases in figure 3.4. It can be seen that the streamwise velocity near the sharp edge has significantly increased for the MRV and LES results of Baek et al. [13]. This is because the ribs installed on both walls cause the flow to follow the ribs along the wall, hit the wide edge, and then become redirected toward the tip region. The increase of streamwise velocity at the tip in our case is not as substantial as the previous work, because the ribs are installed only on the bottom wall.

Since a direct comparison between the current case and the preliminary work is not possible due to the different geometries, wall shear stress distributions along the bottom wall are additionally compared. This comparison is based on two assumptions: (i) the local wall shear stress is highly correlated with the local heat transfer coefficient according to the Reynolds analogy; (ii) the ribs on the upper wall do not significantly affect

the flow characteristics near the bottom wall.

The wall shear stress distributions in the reference and current cases are plotted in figure 3.5. Wall shear stress values were non-dimensionalized using the bulk velocity and hydraulic diameter. The profile is along the bottom surface of the fluid domain, in the spanwise direction. The location of the ribs is denoted by the gray squares. As can be seen, several common characteristics are found. First, local peaks from the RANS analysis are at almost the same locations as those from LES. Although their magnitudes are not completely the same, the prescribed assumption seems to be correct to some extent: ribs on the upper wall do not significantly affect the local flow characteristics near the bottom wall. Second, profiles of the wall shear stress distribution in the region without ribs (i.e. $x/W < 0.4$) are similar in overall shape, aside from the fluctuations from the LES data. However, resultant values from RANS are nearly half of that from LES. This might be due to the lower streamwise velocity, compared to the previous work. In conclusion, the computed flow field from the RANS simulation was validated using previous work, showing satisfactory agreement.

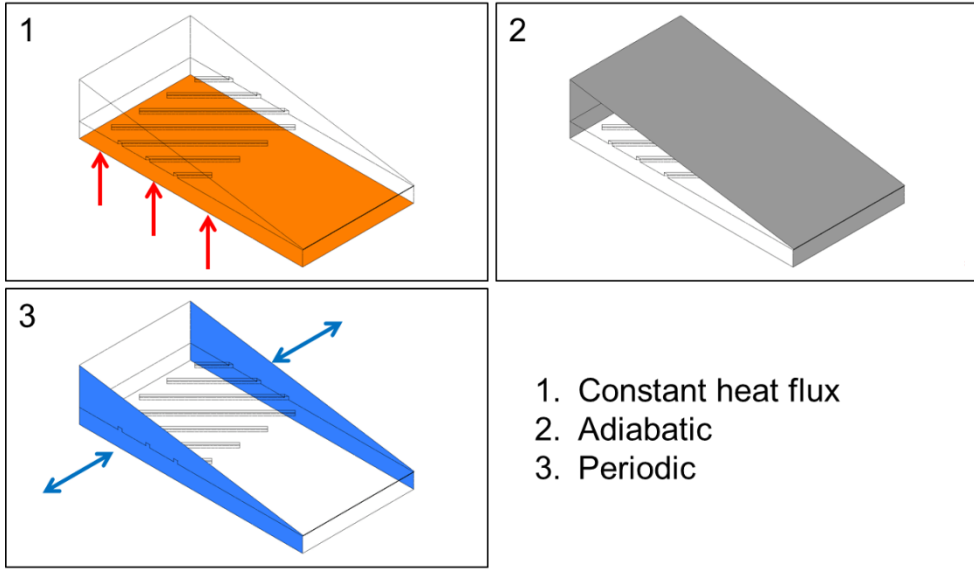


Figure 3.1 Thermal boundary conditions

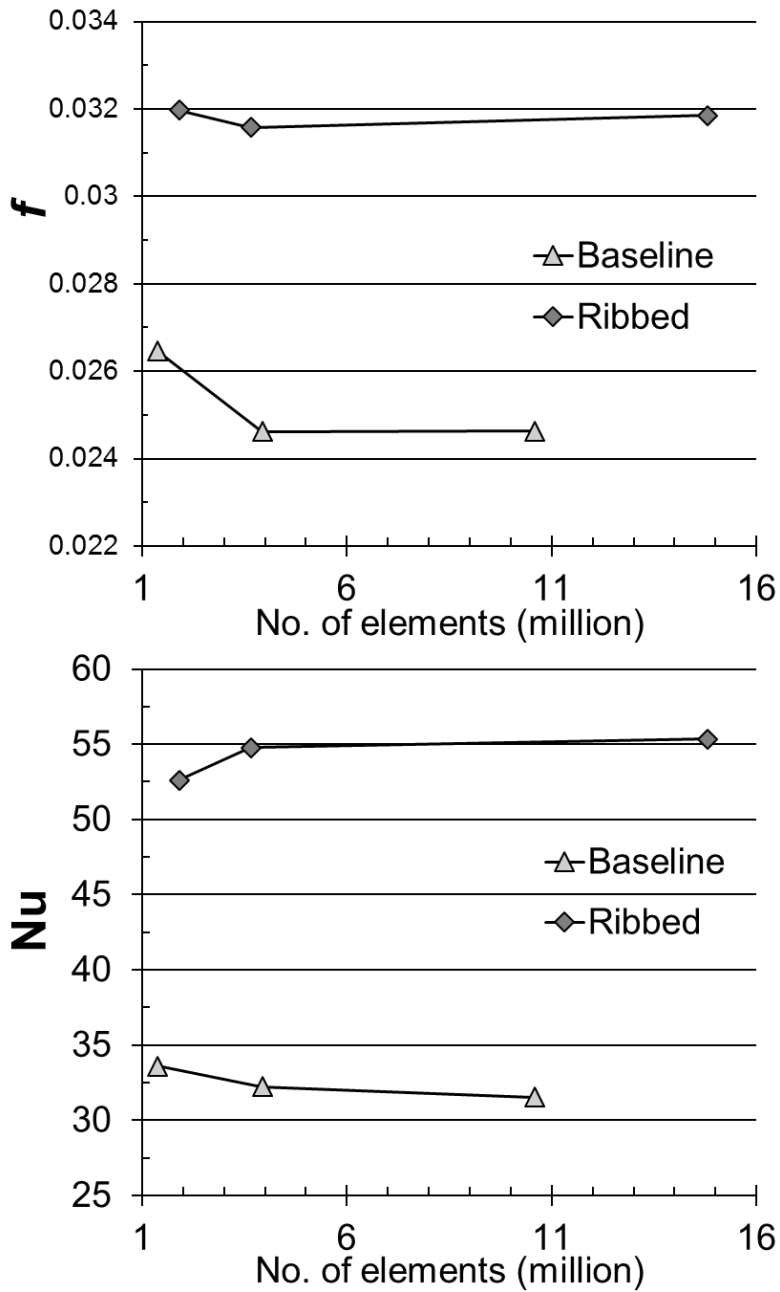


Figure 3.2 Results of grid dependency test

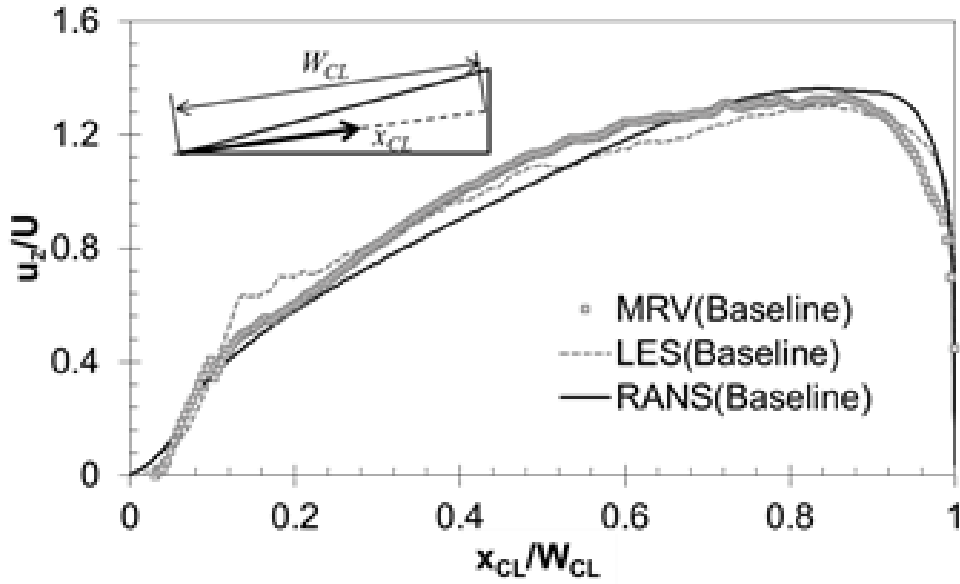


Figure 3.3 Centerline streamwise velocity for the baseline channel (MRV and LES data from Baek et al. [13])

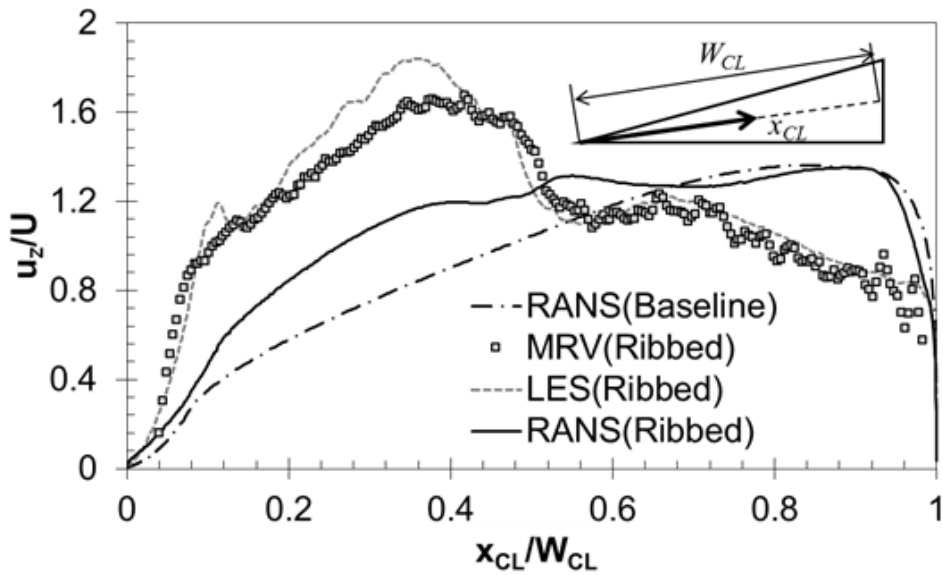


Figure 3.4 Centerline streamwise velocity for ribbed channel (MRV and LES data from Baek et al. [13])

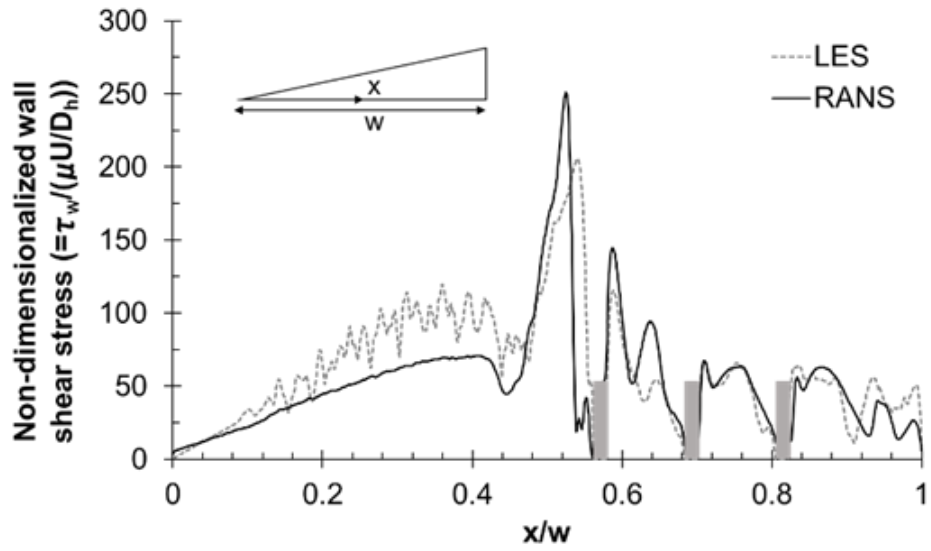


Figure 3.5 Wall shear stress distribution in ribbed channel

Chapter 4. Results and Discussion

4.1. Heat Transfer

Distribution of the non-dimensional surface temperature at each section in the baseline channel is shown in figure 4.1 for $Re \# = 18,400$. The flow is from top to bottom, with the sharp edge at the right side. In section 1, the temperature contour lines are almost perpendicular to the flow direction. This is the beginning of the test section, and it is an area where the flow is developing. Thus, the temperature increases in the streamwise direction. After that, in section 2 where $z/D_h = 17 \sim 22$, the contour lines gradually become parallel with the flow direction. Finally in section 3, especially in the region of $z/D_h = 35 \sim 37$, the contour lines are parallel to the flow direction, meaning there is no more Θ change of the heated surface. This shows that the flow becomes thermally fully developed at section 3.

In addition, it can be seen that the temperature at the sharp edge is higher than the core region in all three sections. The increase in Θ is quite abrupt at the sharp edge. According to Baek et al. [13], the flow becomes laminar in this region because the flow velocity is small. In other words, the cooling flow

rate decreases, leading to less heat transfer and higher temperatures.

Figure 4.2 shows the span-averaged Nusselt numbers with z/D_h for the six Reynolds numbers in the baseline channel. In order to calculate the Nusselt number, the heat flux value from the CFD results is used. The numerical method has been validated by velocity and temperature fields. The symbols in figure 4.2 are from data measured by thermocouples, and the lines are from data measured by IR thermography. The averaged Nusselt numbers converged in section 3 for all Reynolds numbers, confirming that the flow is thermally fully developed.

The average Nusselt number in the fully developed region is plotted against the Reynolds number in figure 4.3. The trend is similar to the correlation derived by Leung et al. [9]. It should be noted that Leung's correlation was obtained in an isosceles triangular cross-section with an apex angle between 15° and 90° , at Reynolds numbers between 7,000 and 20,000. This is likely the reason that the current values show a difference of up to 9% compared to the correlation. The correlation between averaged Nusselt number and Reynolds number that gives the best fit can be expressed as:

$$\text{Nu} = 0.0295\text{Re}^{0.73} \dots\dots\dots \text{Equation 4.1}$$

The effect of the ribs on the heat transfer at the triangular channel is shown in figure 4.4. The localized Nusselt number distribution within the fully developed region, section 3, is shown for a Reynolds number of 11,900. As mentioned earlier, the flow becomes fully developed when z/D_h is 35 or higher. Therefore, data is extracted and processed for z/D_h between 34 and 37. The upper part of the image corresponds to the sharp edge, and the flow is moving from left to right.

Heat transfer peaks are located at the rib edges which are facing the upstream direction. This is due to flow impingement, before it is redirected by the ribs. As the flow travels between the ribs along the surface, the heat transfer increases immediately downstream of the rib edges. The ribs themselves also have a fair amount of heat transfer. In addition, there is a section in which the Nusselt number slightly increases, between the ribs and the sharp edge. This is due to increased streamwise velocity in this area, as evidenced by Baek et al. [13].

Figure 4.5 shows the Nusselt number distribution for four streamwise

lines in the space between two ribs, which we will describe as upstream and downstream ribs. Local heat transfer on the surface between two ribs has been studied by numerous previous works, including Ahn et al. [14] and Aliaga et al. [28]. The Nusselt number trend in line **a** is similar to that of previous studies. The first strong peak is due to the reattachment of the separated flow resulting from the upstream rib. Thereafter, it tends to decrease gradually along the flow direction, due to boundary layer development. The second peak occurs immediately before the downstream rib, due to the small vortex caused by the recirculation zone in front of this rib. Although the slanted direction of ribs in this study is different from the perpendicular orientation of the previous studies, the heat transfer characteristics along line **a** show similar trends. This implies that the flow structure along line **a** is similar to that of the perpendicular ribs. The heat transfer characteristics along line **b** are different. There is a small peak just behind the upstream rib, a stronger peak between the two ribs, and another small peak just before the downstream rib. The Nusselt number profile along line **c** displays a broad peak near the middle. Along line **d** there is no prominent peak, except for a slight bump toward the downstream rib. The reason for these heat transfer distributions

are tied to the convective flow structure, which will be explained hereafter.

In order to find out the reason why the Nusselt number distributions are so different along each line, flow structures from CFD (especially the vortices induced by the ribs), are further investigated. Since the flow near the ribbed wall is highly three-dimensional, two-dimensional streamlines would be insufficient to properly capture significant flow structures such as vortices. Here, we adopt the swirling strength criterion to visualize the 3D vortices. The swirling strength is defined as the imaginary part of two complex eigenvalues of the velocity gradient tensor, and it quantifies the strength of the local swirling motion [29]. Previous researchers such as Zhu et al. [30] also visualized vortex core regions in the flow near a 45° ribbed wall.

Figure 4.6 illustrates the vortex core regions near the ribs. These regions are defined as the iso-surface with swirling strength of 2165s^{-1} , and they are colored based on the magnitude of the local velocity, normalized by averaged velocity for better interpretation. Zhu et al. [30] showed similar results, where the vortex core regions stretched from an upstream rib to a downstream rib, at an angle of about 30° with respect to the streamwise direction. A further in-depth analysis of these vortices will be done here, since it was not provided

in the previous study.

Four different vortices can be identified from figure 4.6: V_1 , V_2 , V_3 , and V_4 . V_1 is the strongest vortex that is generated from the recirculation zone behind the backward facing step of the upstream rib. V_2 is a small secondary vortex generated between V_1 and the backside of the upstream rib. Its rotational direction is opposite that of V_1 . V_3 is generated by the flow separation at the top upstream edge of the upstream rib. V_4 is due to the recirculation zone in front of the downstream rib. It can be seen that V_1 , V_2 , and V_3 drift downstream at an angle of 30° , whereas V_4 always remains attached to the front side of the rib. The detailed evolution of these vortices is shown in figure 4.7.

Figure 4.7 shows the streamwise locations of each vortex in three planes. The dark regions represent locations where swirling motion occurs. 2D streamlines were overlaid in the figures to help comprehend the flow structure. In line **a**, it becomes obvious that V_1 is due to the main recirculation zone immediately behind the upstream rib. Although V_2 is not captured clearly in the figure because of the low resolution, V_3 and V_4 can be clearly noticed. In line **b**, the locations of the vortices start to change. V_1 is no longer attached to

the backside of the upstream rib, but drifts toward the downstream rib. V_2 develops, and also becomes detached from the upstream rib and drifts downstream, as does V_3 . Only V_4 remains at the same location, attached to the front of the downstream rib. By the line **c** location, V_1 has already reached the downstream rib, and V_2 has diminished in strength and is no longer visible. The detached V_3 is still drifting towards the downstream rib, and is the only swirling region between the two ribs. The location of V_4 still remains the same, but its strength has decreased. It is noteworthy that the clockwise rotation V_1 seems to have merged into the clockwise rotation V_4 , and is no longer flowing over the downstream rib, as can be seen from figures 4.6 and 4.7. By this point, the flow seems to be moving along the rib, not over it.

By comparing the contours of swirling strength at each plane and the Nusselt number distributions, a good agreement between the swirling strength and Nusselt number peaks can be found. For further in-depth analysis on how the instantaneous flow structures affect the local heat transfer characteristics, experimental methods such as PIV or numerical methods such as LES or DNS should be employed. We only infer here that the impinging or lift-off motion from the surface, induced by the vortices, results in high and low heat transfer

coefficients.

Figure 4.8 shows the average normalized Nusselt number distributions in the baseline and ribbed channels at the sharp edge, from the experiments. Nusselt numbers are first averaged in the streamwise direction at the fully developed flow section for $z/D_h = 34 - 37$. Then, it is normalized by Nu_0 obtained from the Dittus-Boelter equation. The graph shows a section of $x/w = 0 - 0.4$ at the corner, where the ribs are not present.

The Nusselt number for the ribbed channel is more than twice higher than that of the baseline, demonstrating that the rib turbulators promote the heat transfer at the sharp trailing edge. This is caused by a combination of flow blockage effect from the ribs, and secondary flow toward the tip [13]. However, at the very tip for $x/w = 0 - 0.1$, the flow is laminar due to the dominant boundary layer effects even with the ribs, and thus the Nusselt number is small. It increases for both channels with x/w , meaning that the heat transfer is more active at the core region, as expected. In the case of the ribbed channel, heat transfer increases significantly beyond $x/w = 0.12$, due to the increase in flow velocity and turbulence intensity [13]. This rapid increase of heat transfer in the ribbed channel is in good agreement with

previous studies.

4.2. Pressure Losses

The friction factors in the baseline and ribbed channel have been measured for various Reynolds numbers. Figure 4.9 shows the experimentally measured friction factors for Reynolds numbers between 9,000 and 20,000. The baseline channel results show a relatively sharp decrease with Reynolds number, compared to the correlation by Capobianchi et al. [31]. This discrepancy could be due to the fact that we are not using an isosceles triangular channel, but a right triangular channel. The friction factor in the baseline channel is also about 20 – 30% lower than the Blasius solution for all Reynolds numbers. Compared to a smooth circular tube, a triangular channel has lower shear stress in the sharp corner, due to the thicker viscous sublayer [32], and results in a lower friction factor.

The friction factor in the ribbed channel is about 10 – 15% higher than that of the baseline channel due to the flow obstruction by the ribs, as expected. The rib channel friction factor is also higher than that of the Blasius solution at low Reynolds numbers, but smaller at higher Reynolds numbers.

The friction factor was previously measured in the same triangular channel, but with ribs placed on both pressure and suction side surfaces [13]. According to this previous study, the friction factor was about 0.027 at a Reynolds number of 14,000. The friction factor in our single-side ribbed channel is essentially the same at 0.028, thus showing good agreement. In addition, the friction factor from the CFD and experiment in the ribbed channel also showed difference within 5%.

4.3. Thermal Performance

The overall thermal performance (F) can be defined as:

$$F = \frac{\overline{Nu}}{\overline{Nu_{base}} \left(\frac{f}{f_{base}} \right)^{\frac{1}{3}}} \dots\dots\dots Equation 4.2$$

Table 4.1 shows the thermal performance of the ribbed channel for Reynolds numbers between 9,000 and 12,000. The Nusselt number and friction factor in the baseline channel are calculated from correlations for the Reynolds number, based on the experimental results. For higher Reynolds number, the thermal performance in the ribbed channel increases slightly, and

in all three cases the thermal performance values are near 2.

4.4. Uncertainty

Uncertainty analysis is performed using the method described by Moffat [27]. The uncertainty in local heat transfer coefficient depends on (i) errors in measuring bulk air temperature with thermocouples, (ii) errors in calculating heat flux, and (iii) error in counts for the measurement of heated surface temperature with IR thermography. The error in the thermocouples is 0.1K. When the temperature of the heated surface is measured, the temperature varied between $\pm 0.2\text{K}$. The error in the heat flux calculated by ANSYS is 7%. Based on these error sources, the error of the Nusselt number error is estimated to be approximately about $\pm 8\%$.

The uncertainty in the mean flow measurement results in $\pm 3\%$ uncertainty of the associated Reynolds number at the test section. Finally, the uncertainty in the friction factor f is estimated to be $\pm 9\%$.

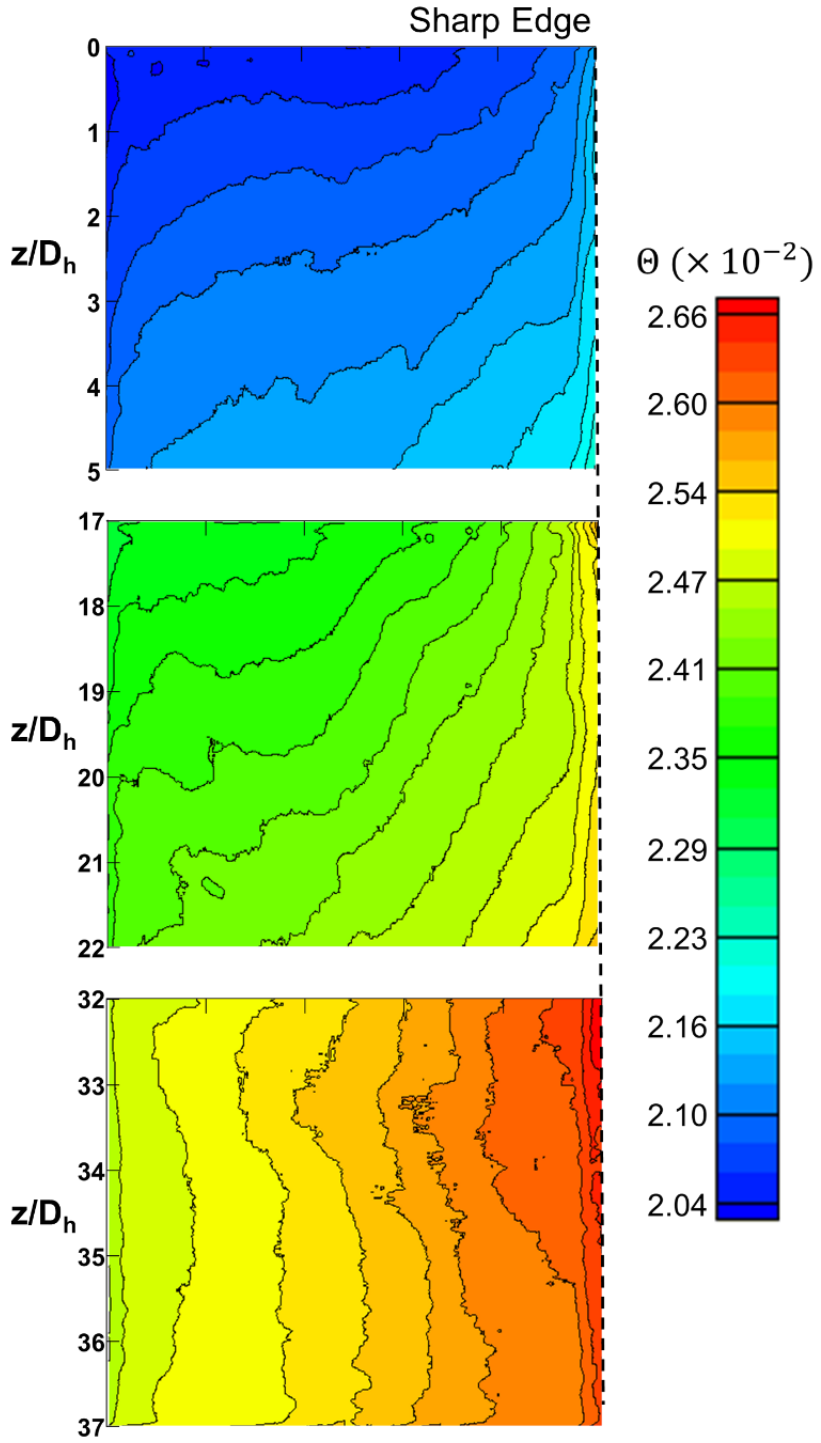


Figure 4.1 Non-dimensional temperature distribution in the baseline channel

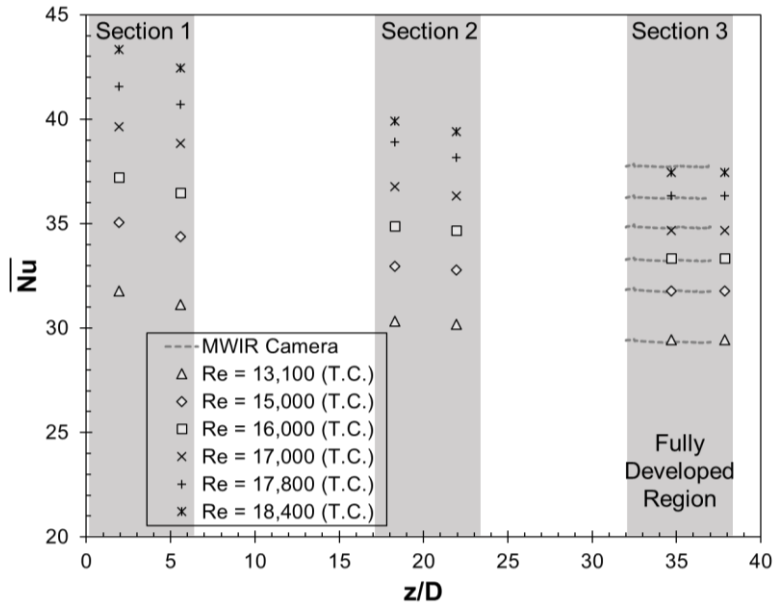


Figure 4.2 Averaged Nusselt number along streamwise direction in baseline channel

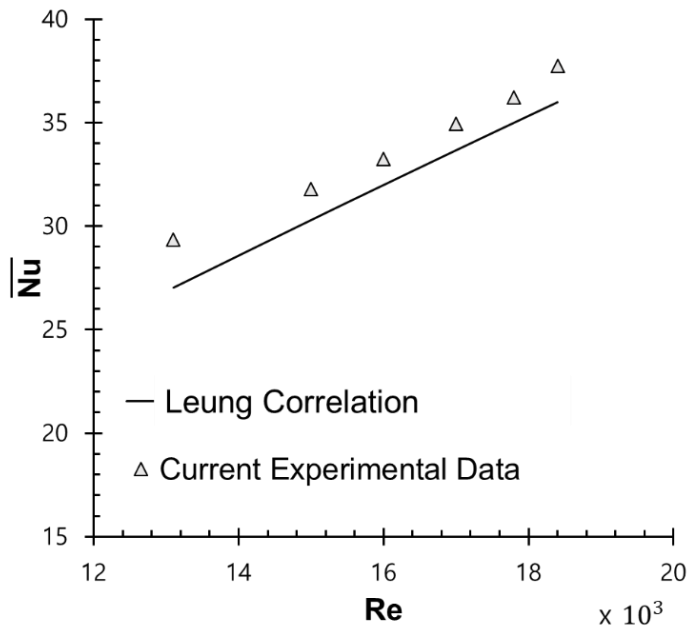


Figure 4.3 Averaged Nusselt number in baseline channel at fully developed region

Sharp Edge

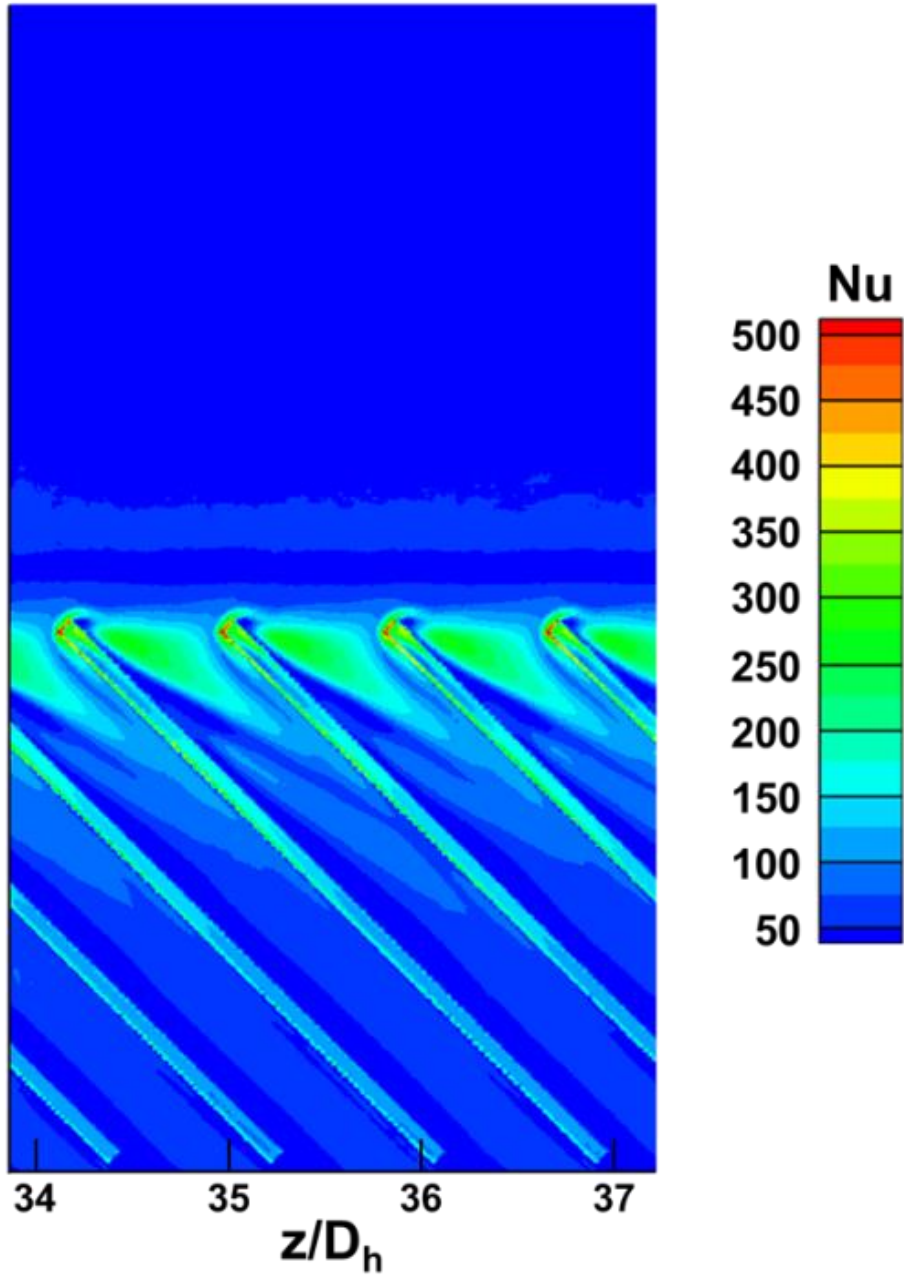


Figure 4.4 Local Nusselt number contour in ribbed channel

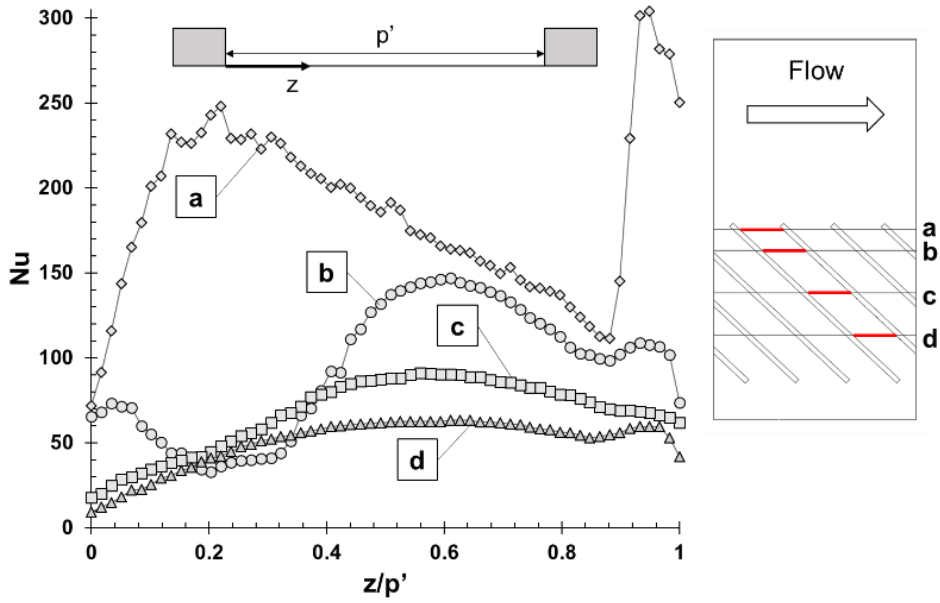


Figure 4.5 Local Nusselt number distribution between the ribs

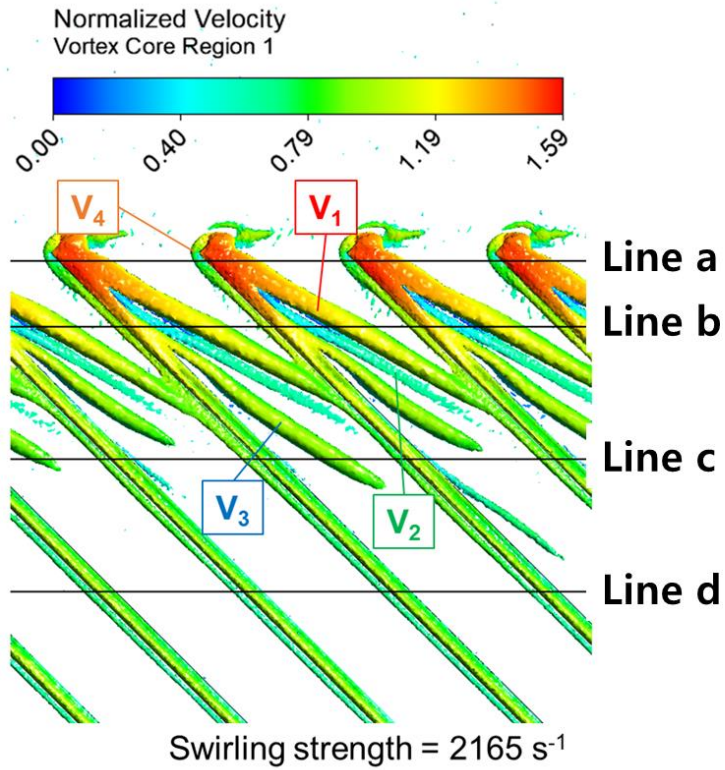


Figure 4.6 Vortex core region in ribbed channel near the ribs

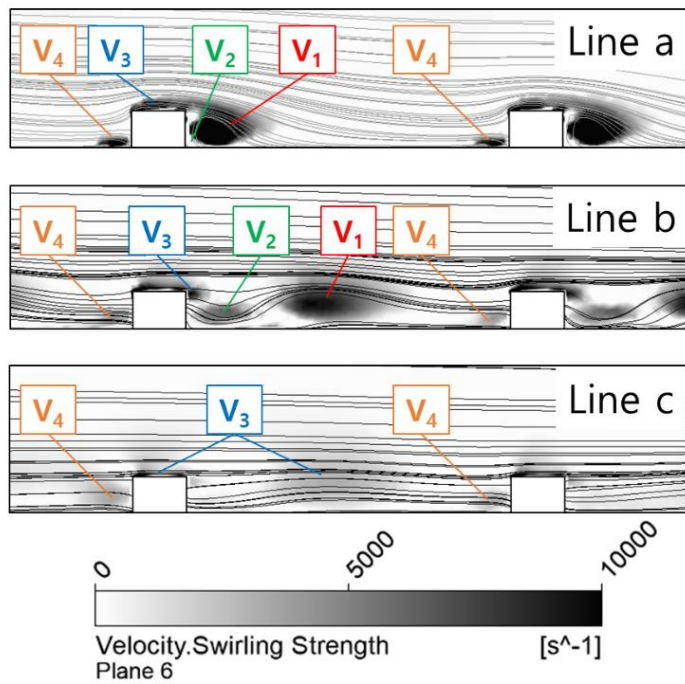


Figure 4.7 2D distribution of swirling strength in ribbed channel

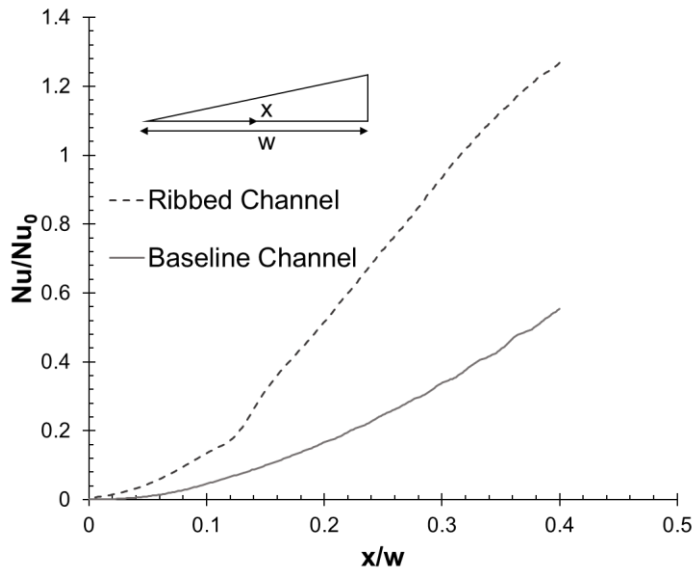


Figure 4.8 Normalized averaged Nusselt number near the sharp edge

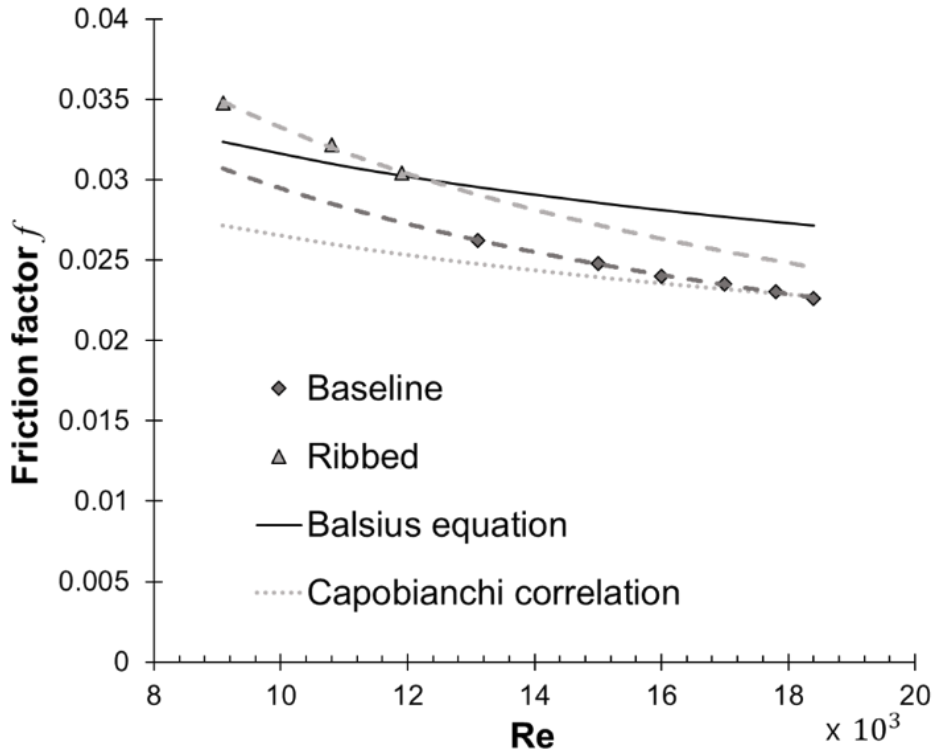


Figure 4.9 Friction factor in baseline and ribbed channel

Table 4.1 Thermal performance in ribbed channel

| Reynolds number | Thermal performance |
|-----------------|---------------------|
| 9,100 | 1.89 |
| 10,800 | 1.90 |
| 12,000 | 1.99 |

Chapter 5. Conclusion

An experimental and numerical study has been performed to investigate the heat transfer and pressure drop in a right triangular channel, which represents the trailing edge internal cooling passage of a turbine blade. Two channels have been investigated: a ribless baseline channel and ribbed channel. The ribs are placed at a 45° angle with respect to the flow. The Reynolds number based on the channel hydraulic diameter range from 9,100 to 18,500. Non-uniformities in the heat flux due to conduction are corrected by a RANS conjugate heat transfer calculation. The numerical simulations have been validated with velocity fields from experimental and LES results of a previous study [13]. Infrared thermography is applied to obtain distributions of non-dimensional temperature and Nusselt number. Heat transfer characteristics in the ribbed channel are explained using the flow structure. The major conclusions are as follows:

- The baseline channel has higher surface temperature at the corner, due to the small amount of convective flow.

- By installing ribs, a significant amount of convective heat transfer occurs near the upstream rib edge.
- The downstream spread of convective heat transfer is closely tied with the channel vortical flow structure.
- Although the convective heat transfer is relatively small at the sharp corner, it is still significantly higher than that of the baseline channel. The Nusselt number increases by more than a factor of two with the ribs, due to the increased streamwise flow in the ribless region near the corner. This is caused by a combination of flow blockage effect from the ribs, and secondary flow towards the corner.
- Although the pressure loss and friction increase slightly, the overall thermal performance, represented by the average Nusselt number with respect to the friction factor, increases by a factor of two with the ribs.

Acknowledgements

The numerical simulation was performed by Seungwon Suh, an undergraduate student in the mechanical engineering department at Seoul National University.

Bibliography

- [1] Naik, S., Retzko, S., Gritsch, M., and Sedlov, A., 2014, "Impact of Turbulator Design on the Heat Transfer in a High Aspect Ratio Passage of a Turbine Blade," Proceedings. ASME Turbo Expo 2014, Düsseldorf, Germany, GT2014-25841.
- [2] Han, J. C., 2004, "Recent Studies in Turbine Blade Cooling," International Journal of Rotating Machinery, 10(6), pp. 443-457.
- [3] Cunha, F., and Chyu, M. K., 2006, "Trailing-Edge Cooling for Gas Turbines," Journal of Propulsion and Power, 22(2), pp. 286-300.
- [4] Horbach, T., Schulz, A., and Bauer, H. J., 2011, "Trailing Edge Film Cooling of Gas Turbine Airfoils—External Cooling Performance of Various Internal Pin Fin Configurations," ASME J Turbomach., 133(4), p. 041006.
- [5] Martini, P., Schulz, A., and Bauer, H. J., 2006, "Film Cooling Effectiveness and Heat Transfer on the Trailing Edge Cutback of Gas Turbine Airfoils with Various Internal Cooling Designs," ASME J Turbomach., 128(1), pp. 196-205.
- [6] Martini, P., Schulz, A., Bauer, H. J., and Whitney, C., 2006, "Detached Eddy Simulation of Film Cooling Performance on the Trailing Edge Cutback of Gas Turbine Airfoils," ASME J Turbomach., 128(2), pp. 292-299.
- [7] Schneider, H., von Terzi, D., and Bauer, H. J., 2010, "Large-Eddy Simulations of Trailing-Edge Cutback Film Cooling at Low Blowing Ratio," International Journal of Heat and Fluid Flow, 31(5), pp. 767-775.

- [8] Eckert, E. R. G., and Irvine, T., 1960, "Pressure Drop and Heat Transfer in a Duct with Triangular Cross Section." *ASME J Heat Trans.*, 82, pp. 125 – 138.
- [9] Leung, C., Wong, T., and Kang, H., 1998, "Forced Convection of Turbulent Flow in Triangular Ducts with Different Angles and Surface Roughnesses," *Heat and Mass Transfer*, 34(1), pp. 63-68.
- [10] Carlson, L., and Irvine, T., 1961, "Fully Developed Pressure Drop in Triangular Shaped Ducts," *ASME J Heat Trans.*, 83(4), pp. 441-444.
- [11] Hiromoto, U., Yuji, S., and Hiromichi, F., 1982, "Turbulence Measurements and Mass Transfer in Fully Developed Flow in a Triangular Duct with a Narrow Apex Angle," *International Journal of Heat and Mass Transfer*, 25(5), pp. 615-624.
- [12] Daschiel, G., Frohnäpfel, B., and Jovanović, J., 2013, "Numerical Investigation of Flow through a Triangular Duct: The Coexistence of Laminar and Turbulent Flow," *International Journal of Heat and Fluid Flow*, 41, pp. 27-33.
- [13] Baek, S., Lee, S., Hwang, W., and Park, J. S., 2019, "Experimental and Numerical Investigation of the Flow in a Trailing Edge Ribbed Internal Cooling Passage," *ASME J Turbomach.*, 141(1), p. 011012.
- [14] Ahn, J., Choi, H., and Lee, J. S., 2005, "Large Eddy Simulation of Flow and Heat Transfer in a Channel Roughened by Square or Semicircle Ribs," *ASME J Turbomach.*, 127(2), pp. 263-292.
- [15] Astarita, T., and Cardone, G., 2003, "Convective Heat Transfer in a Square Channel with Angled Ribs on Two Opposite Walls," *Experiments in Fluids*, 34(5), pp. 625-634.

- [16] Tanda, G., 2011, "Effect of Rib Spacing on Heat Transfer and Friction in a Rectangular Channel with 45° Angled Rib Turbulators on One/Two Walls," *International Journal of Heat and Mass Transfer*, 54(5-6), pp. 1081-1090.
- [17] Peng, W., Jiang, P. X., Wang, Y. P., and Wei, B. Y., 2011, "Experimental and Numerical Investigation of Convection Heat Transfer in Channels with Different Types of Ribs," *Applied Thermal Engineering*, 31(14-15), pp. 2702-2708.
- [18] SriHarsha, V., Prabhu, S., and Vedula, R., 2009, "Influence of Rib Height on the Local Heat Transfer Distribution and Pressure Drop in a Square Channel with 90° Continuous and 60° V-Broken Ribs," *Applied Thermal Engineering*, 29(11-12), pp. 2444-2459.
- [19] Rallabandi, A. P., Yang, H., and Han, J. C., 2009, "Heat Transfer and Pressure Drop Correlations for Square Channels with 45 Deg Ribs at High Reynolds Numbers," *ASME J Heat Trans.*, 131(7), p. 071703.
- [20] Alkhamis, N. Y., Rallabandi, A. P., and Han, J. C., 2011, "Heat Transfer and Pressure Drop Correlations for Square Channels with V-Shaped Ribs at High Reynolds Numbers," *ASME J Heat Trans.*, 133(11), p. 111901.
- [21] Saxer-Felici, H., Naik, S., and Gritsch, M., 2013, "Heat Transfer Characteristics of a Blade Trailing Edge with Pressure Side Bleed Extraction," *Proceedings. ASME Turbo Expo 2013*, San Antonio, Texas, USA, GT2013-95003.
- [22] Coletti, F., Scialanga, M., and Arts, T., 2012, "Experimental Investigation of Conjugate Heat Transfer in a Rib-Roughened Trailing Edge Channel with Crossing Jets," *ASME J Turbomach.*, 134(4), p. 041016.

- [23] Won, S., Burgess, N., Peddicord, S., and Ligrani, P., 2004, "Spatially Resolved Surface Heat Transfer for Parallel Rib Turbulators with 45 Deg Orientations Including Test Surface Conduction Analysis," *ASME J Heat Trans.*, 126(2), pp. 193-201.
- [24] Gustavsson, J., Hylén, J., Kinell, M., and Utriainen, E., 2010, "Window Temperature Impact on Ir Thermography for Heat Transfer Measurements," *Proceedings. AIAA-2010-0670*, 48th AIAA Aerospace Sciences Meeting, Orlando, FL.
- [25] Kawamura, H., Ohsaka, K., Abe, H., and Yamamoto, K., 1998, "Dns of Turbulent Heat Transfer in Channel Flow with Low to Medium-High Prandtl Number Fluid," *International Journal of Heat and Fluid Flow*, 19(5), pp. 482-491.
- [26] Lee, S., and Hwang, W., 2019, "Development of an Efficient Immersed-Boundary Method with Subgrid-Scale Models for Conjugate Heat Transfer Analysis Using Large Eddy Simulation," *International Journal of Heat and Mass Transfer*, 134, pp. 198-208.
- [27] Moffat, R. J., 1988, "Describing the Uncertainties in Experimental Results," *Experimental Thermal and Fluid Science*, 1(1), pp. 3-17.
- [28] Aliaga, D., Lamb, J., and Klein, D. E., 1994, "Convection Heat Transfer Distributions over Plates with Square Ribs from Infrared Thermography Measurements," *International Journal of Heat and Mass Transfer*, 37(3), pp. 363-374.
- [29] Holmén, V., 2012, "Methods for Vortex Identification," *Master's Theses in Mathematical Sciences*.
- [30] Zhu, J., Gao, T., Li, J., Li, G., and Gong, J., "The Effect of Vortex Core Distribution on Heat Transfer in Steam Cooling of Gas Turbine Blade Internal Ribbed Channels," *Proceedings. ASME Turbo Expo 2014, Düsseldorf, Germany, GT2014-25324*.

- [31] Capobianchi, M., Irvine, T., and Thomas, F., 1997, "Triangular Ducts, Flow and Heat Transfer," International Encyclopedia of Heat & Mass Transfer, CRC Press, Boca Raton.
- [32] Domaschke, N., von Wolfersdorf, J., and Semmler, K., 2012, "Heat Transfer and Pressure Drop Measurements in a Rib Roughened Leading Edge Cooling Channel," ASME J Turbomach., 134(6), p. 061006.

요약

가스터빈 블레이드 형상으로 인해, 블레이드 후연의 내부냉각 유로는 매우 좁다. 이로 인해 컷 아웃 슬롯 냉각기법이 적용되지 않으면 샤프 엣지 형상이 생기게 되며, 이 부분에서는 내부냉각이 원활하게 일어나지 않는 경우가 많다. 따라서 샤프 엣지 형상을 포함한 블레이드 후연의 냉각성능을 관측하는 연구가 필요하다. 본 연구는 블레이드 후연을 형상화한 삼각채널에서의 열전달 및 압력강하를 실험적으로 측정하였다. 삼각채널의 꼭지각은 9° 이며, 45° 립의 유무에 따른 두가지 채널에서 실험을 진행하였다. 적외선 카메라를 이용한 실험적인 방법으로 열전달을 측정하였으며, 열전도 현상으로 생기는 오차는 RANS 를 통한 수치해석을 통해 보정하였다. 수치해석은 선행연구의 속도장, 마찰 계수 및 온도장을 이용하여 검증하였다.

열전달 현상은 너셀 수 분포를 통해 관측되었다. 본 연구 결과에서는 립을 설치함으로써 채널 내의 평균 너셀 수가 2 배로 증가했음을 보였다. 특히, 향상된 열전달 성능은 채널 내의 유동 구조 및 와류 구조와 상관관계를 보였다. 립으로 인해 생기는 2 차 유동이 샤프 엣지 구간으로의 유량을 증가시키면서, 샤프 엣지 구간에서의 열전달 현상을 대폭 증가시킴을 확인하였다. 마찰 계수 역시 립을 설치함으로써 조금 증가했지만, 열 성능을 계산했을 때 립을 설치하는 것이 약 2 배정도 높은 성능 결과를 보여줬다.

주요어: 가스터빈 블레이드, 뒷전, 샤프 엣지, 삼각 채널, 열전달, 립

학번: 2018-23025

감사의 글

대학원에 입학 이후 두번째 겨울을 맞이하며 석사 졸업 논문을 마무리하게 되었습니다. 2년의 연구실 생활에는 즐거운 점도 많았지만 많은 어려운 점들도 많았습니다. 그럴 때 마다 항상 주변에 많은 분들이 도움과 위로를 건네 주신 덕분에, 갑진 졸업 논문을 완성할 수 있게 되었습니다. 이 자리를 빌려 감사의 글을 전하고자 합니다.

가장 먼저 저의 지도교수님이신 황원태 교수님께 감사의 글을 전하고 싶습니다. 방황을 많이 하고 있는 저를 연구실 인턴으로서 연구에 첫 발을 내딛게 해주셨으며, 석사 과정을 밟으면서 부딪힌 여러 난관들을 같이 해결해 주시려 노력하셨습니다. 2년의 시간 동안 진심을 다해 도와주시고 신경을 써주신 황원태 교수님께 감사의 글을 전합니다.

다음으로 물심양면으로 지원해주고 응원해준 가족에게 감사의 글을 드립니다. 정신없는 연구실 생활을 하며 자주 연락드리지 못했지만, 언제나 저를 믿어주고 응원해줘서 석사 학위를 무사히 받을 수 있게 되었습니다. 아버지, 어머니, 누나 감사하고 사랑합니다.

마지막으로 같이 동거동락한 연구실 동료들에게 감사의 글을 전합니다. 1기 생으로서 항상 열정적으로 연구를 하며 많은 조언을 해준 승찬이 형과 훈상이 형 그리고 준영이 형, 대학원 생활에 아낌없이 조언을 해준 구원이 형, 굵은 일을 도맡아 해준 재현이 형, 깊은 생각을 가지며 항상 고민하는 한준이 형, 기분 좋은 미소를 띄는 규호 형, 동기로서 많은 도움을 준 현균이 형, 자신의 위치에서 최선을 다해 연구를 하는 무성이와 형우 형, 그리고 힘든 일을 같이 하며 지칠 때 항상 웃음을 주는 창은이 형 감사합니다. 또한, 연구실 인턴으로 짧은 시간을 함께했지만 자극을 많이 준 상준이 형과 진언이, 그리고 같이 논문을 쓰며 묵묵히 자신의 일을 열심히 했던 승원이에게도 감사의 글을 전합니다.